# Synthesis, Structure, and Properties of Bi3.25Pr0.75Ti2.97V0.03O12 Ferroelectric Ceramics

**3 AUTHORS:**

Hongchu Du
Forschungszentrum Jülich
**22** PUBLICATIONS **180** CITATIONS

SEE PROFILE

Sebastian Wohlrab
Leibniz Institute for Catalysis
**55** PUBLICATIONS **509** CITATIONS

SEE PROFILE

Stefan Kaskel
Technische Universität Dresden
**295** PUBLICATIONS **6,777** CITATIONS

SEE PROFILE

# Synthesis, Structure, and Properties of $Bi_{3.25}Pr_{0.75}Ti_{2.97}V_{0.03}O_{12}$ Ferroelectric Ceramics

## Hongchu Du, Sebastian Wohlrab, and Stefan Kaskel*

*Department of Inorganic Chemistry, Technical University of Dresden, Mommsenstrasse 6, 01069 Dresden, Germany*

Praseodymium and vanadium cosubstituted $Bi_4Ti_3O_{12}$ was synthesized using a modified citrate-gel method. The crystallization was promoted by the oxidation of residual carbon produced by decomposition of $-CH_x$ groups resulting in a crystallization temperature as low as 450 °C. The as-synthesized powder consisted of uniform spherical particles with a mean size of 57 nm and a standard deviation of 14 nm. The ceramic prepared from the as-synthesized powder at 900 °C consisted mainly of randomly arranged platelets with a thickness of 200 nm. The Rietveld refinement in the orthorhombic space group $Aba2$ for the as-prepared $Pr^{3+}$ and $V^{5+}$ cosubstituted $Bi_4Ti_3O_{12}$ resulted in a convergent refinement ($R_{wp} = 5.01\%$). The remanent polarization ($2P_r$) and coercive field ($2E_c$) values measured at room temperature with a maximum electric field of $\pm300$ kV/cm were 35 $\mu C/cm^2$ and 148 kV/cm, respectively. The ceramic has a very low ohmic conductivity, and the leakage current density is below 1 $\mu A/cm^2$ up to 200 kV/cm. No profound fatigue was observed after switching over $10^8$ cycles. The evolution of $2E_c$, $2P_r$, $P_{max}$ (maximum polarization), and $P_{max}/P_r$ with $E_{max}$ (maximum electric field) is discussed using an ideal and a four components ferroelectric capacitor model. The observed linear relationship between $P_{max}/P_r$ and $E_{max}$ provides the possibility to calculate the field independent dielectric constant (282) and nonremanent polarization (2.7 $\mu C/cm^2$ at $E_{max} = 300$ kV/cm) for the ceramic studied.

## 1. Introduction

A variety of promising applications, such as ferroelectric nonvolatile memories,[1,2] micro-electromechanical systems,[3] tunable high-frequency devices,[4] and integrated photonics,[5] have recently stimulated intensive interest in ferroelectric materials. Aurivillius type bismuth layer-structured perovskite oxide ferroelectrics have attracted considerable attention due to their environmentally friendly composition. These compounds possess a general formula of $(Bi_2O_2)^{2+}(A_{n-1}B_nO_{3n+1})^{2-}$, where A are mono-, di-, or trivalent ions or mixtures of them, B are tetra-, penta-, or hexavalent ions, and $n$ represents the number of $BO_6$ octahedra in the pseudo-perovskite slab and can be 1, 2, 3, 4, and so forth.[6] In these crystal structures, the pseudo-perovskite slabs, $(A_{n-1}B_nO_{3n+1})^{2-}$, are interleaved with bismuth oxide layers, $(Bi_2O_2)^{2+}$, along the $c$ axis. $SrBi_2Ta_2O_9$ (SBT) is probably the first one of the most intensively studied bismuth layer-structured ferroelectrics (BLSFs) with $n = 2$ characterized by its excellent endurance, long retention time, and low leakage currents.[7] However, SBT has been criticized for its disadvantages of low remanent polarization and high processing temperature restricting practical applications.[8−12] $Bi_4Ti_3O_{12}$ is also a member of BLSFs ($n = 3$), and ferroelectricity in single crystals and ceramic forms was first reported by Uitert and Egerton[13] and Subbarao,[14] respectively, in 1961. The remanent polarization ($P_r$) of $Bi_4Ti_3O_{12}$ single crystals along the $a(b)$ axis was about 50 $\mu C/cm^2$ at room temperature.[15,16] Low crystallization temperatures in between 500 and 650 °C were reported by different authors for the preparation of pure and substituted $Bi_4Ti_3O_{12}$ films.[17−19] The large spontaneous polarization and low processing temperature make $Bi_4Ti_3O_{12}$ more competitive

than SBT for a lead-free ferroelectric material and have inspired intensive studies in the past decade. Improved ferroelectric properties have been reported in substituted $Bi_4Ti_3O_{12}$ films and ceramics, such as A-site isovalent substitution using rare earth cations ($La^{3+}$, $Nd^{3+}$, $Pr^{3+}$, $Sm^{3+}$, etc.),[8,12,20−27] B-site aliovalent substitution using high valence cations (as $V^{5+}$, $W^{6+}$, etc.),[9,10] and cosubstitution of these A and B sites.[11,21,28−31]

Different kinds of techniques have been developed to prepare pure and substituted $Bi_4Ti_3O_{12}$ films, such as pulsed laser deposition (PLD),[8,20] metalorganic chemical vapor deposition (MOCVD),[17,18,28] magnetron sputtering,[19] and chemical solution deposition (CSD).[11,21−23] Conventional solid-state reaction methods have been widely used to prepare $Bi_4Ti_3O_{12}$ ceramics, in which high sintering temperature and long sintering time were required to achieve high density and homogeneous compositions.[9,14,32−34] A number of authors has turned to chemical solution routes, such as citrate gel,[35,36] metalorganic decomposition,[37] coprecipitation,[38] and hydrothermal reactions.[39−43] In comparison with conventional solid-state methods, solution methods have several advantages, such as low processing temperature, the ability to provide better control of composition, homogeneity, purity, and so forth. However, most of the mentioned solution methods are reported for the preparation of pure or monosubstituted $Bi_4Ti_3O_{12}$ ceramics. There is still a need for solution protocols to prepare A- and B-site cosubstituted $Bi_4Ti_3O_{12}$ ceramics. The citrate-gel method has been used to synthesize a large number of multicomponent ceramics and ceramic films, in which desired metal salts were mixed with citric acid to form the corresponding soluble citrate complexes in aqueous solution.[44,45] The aqueous citrate solution is dehydrated to yield an amorphous gelatinous solid that can be crystallized into the desired compounds after firing at elevated temperature. The citrate-gel method has several advantages over

* Corresponding author. E-mail: Stefan.Kaskel@chemie.tu-dresden.de. Phone: 49-351-46333632. Fax: 49-351-46337287.

other chemical solution techniques in terms of preparation of multicomponent materials as stated below. No toxic solvent is used in the citrate-gel process. However, in sol−gel[45] and metalorganic decomposition methods,[37] 2-methoxyethanol, a toxic solvent, has been widely used. As far as coprecipitation and hydrothermal methods are concerned, the citrate-gel method can provide more homogeneous mixing and better stoichiometric control. In coprecipitation and hydrothermal processes, however, it is more difficult to find suitable conditions for the preparation of the desired products if the number of components with different solubility increases.

In this work, we report a modified citrate-gel method to prepare $Pr^{3+}/V^{5+}$ A- and B-site cosubstituted bismuth titanate $Bi_{4-x}Pr_xTi_{3-y}V_yO_{12+y/2}$, ($x = 0.75$, $y = 0.03$, BPTV) ceramics. The structure of the BPTV ceramics was refined using the Rietveld method. The ferroelectric properties of BPTV including hysteresis behavior, saturation characteristics, leakage current density, and fatigue are discussed. Substitution of $Pr^{3+}$ by other rare earth ions is suitable to yield other kinds of cosubstitutions. We are therefore confident our work can be extended for the preparation of various A- and B-site cosubstituted $Bi_4Ti_3O_{12}$ or other BLSFs ceramics.

## 2. Experimental Methods

**2.1. Synthesis.** High purity chemicals were used. Bismuth-(III) citrate (99.99%, Aldrich), praseodymium(III) acetate hydrate (99.9%, Aldrich), vanadium(V) oxide (99.99% metal basis, Alfa Aesar), citric acid hydrate (99.5%, Grüssing GmbH), titanium *n*-butoxide (Ti(O-*n*-Bu)₄, 99%, Acros), acetylacetone (Hacac, 99+%, Acros), aqueous ammonium hydroxide (p.a., 25%, VWR), and ethanol (99%, Berkel AHK, Berlin) were used as starting chemicals without further purification. For preparation of BPTV ($x = 0.75$, $y = 0.03$), 3.41 mmol of bismuth citrate (5% in mole excess), 0.75 mmol of praseodymium acetate hydrate, and 5.3 g of citric acid hydrate were dissolved in a solution of 15 mL aqueous ammonium hydroxide (25%) and 15 mL deionized water at room temperature with magnetic stirring, giving a clear solution (solution 1). The vanadium citrate aqueous solution was prepared by dissolving 0.015 mmol of $V_2O_5$ and 2 g of citric acid hydrate in 5 mL of deionized water above 90 °C (solution 2). 2.97 mmol of Ti(O-*n*-Bu)₄ was mixed with 0.5 mL of Hacac, then 5 mL of ethanol was added to yield a yellowish transparent solution (solution 3). The solutions 2 and 3 were subsequently added to solution 1 at room temperature with magnetic stirring and rinsing with 5 mL of deionized water and ethanol, respectively. A light yellowish transparent precursor solution was obtained. The precursor solution was gradually heated up to 70 °C and maintained over night with mild magnetic agitation for gelation. The gel obtained was further dehydrated at 105 °C for 24 h and carbonized at 320 °C in air for 2 h with a ramp of 1 °C/min. The carbonized precursor was calcined at 450−700 °C for 1 h with a heating ramp of 5 °C/ min to get powder products. The powders were ground with ethanol for 30 min using an agate pestle and mortar and were dried at 90 °C over night. The dried powders were uniaxially pressed into pellets of 8.0 mm in diameter and 1.0−2.0 mm in thickness under a pressure of 800 MPa. The green pellets were sintered in air at 900 °C for 4 h (heating ramp of 5 °C/min) and cooled down. The sintered pellets were polished to a thickness of 0.10−0.12 mm. After covering with electrodes using silver paste, the pellets were annealed at 700 °C for 10 min resulting in fraction-free electrodes. All of the ceramics in this work were prepared from the powder calcined at 550 °C.

**2.2. Characterization.** The X-ray diffraction (XRD) patterns were recorded from 10 to 80° (2θ) on a Stoe Stadi P powder
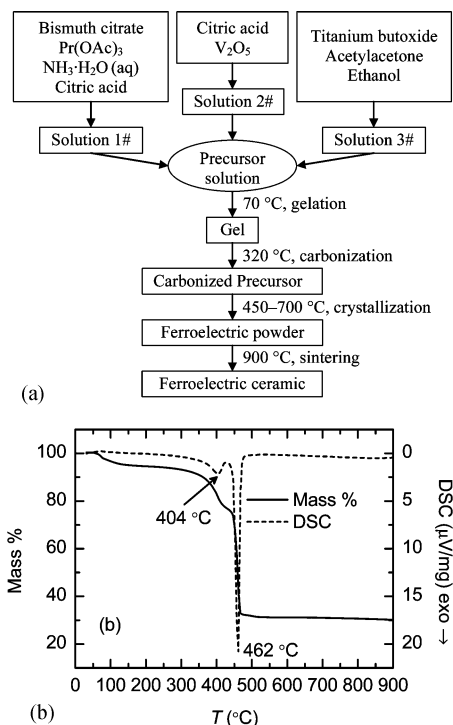


**Figure 1.** (a) Flow diagram of the modified citrate-gel method for preparation of $Pr^{3+}/V^{5+}$ cosubstituted $Bi_4Ti_3O_{12}$ ceramics and (b) TG-DSC plots of the carbonized precursor solid.
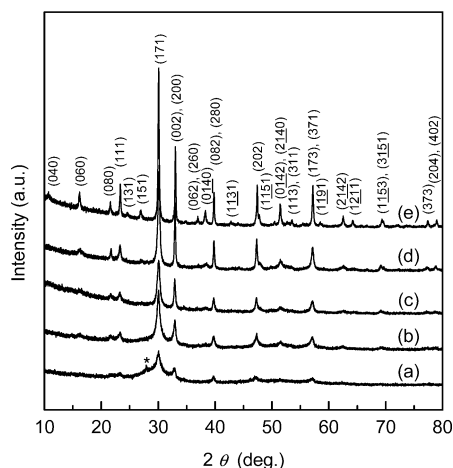
diffractometer equipped with a curved germanium (111) mono-chromator and linear PSD using Cu Kα1 radiation (1.54060 Å) in transmission geometry. The XRD powder pattern from the ceramic sample for the Rietveld refinement was measured with a 2θ step size of 0.01° and a scan speed of 60 s/step. A scan speed of 18.0 s/step was chosen for all of the other XRD patterns. The XRD Rietveld refinement was carried out using the GSAS-EXPGUI program.[46,47] $LaB_6$ was used as a standard to determine the shift of the zero point.

Temperature gradient-differential scanning calorimetry (TG-DSC) data were recorded using a Netzsch STA 409 system in air atmosphere with a heating rate of 5 °C/min. The morphol-ogies of the products were studied using a Zeiss DMS 982 Gemini field emission scanning electron microscope (SEM) equipped with a Noran Voyager energy-dispersive spectroscopy (EDS) system.

The ferroelectric properties were measured on a Radiant Precision LC tester equipped with a Radiant Precision high voltage interface and a Trek 610E high voltage amplifier. $P−E$ hysteresis loops were measured within the range of $E_{max}$ from 10 to 300 kV/cm with a constant increment of 5 kV/cm using a 10 Hz standard bipolar triangular drive waveform. The switching current density was obtained as the first derivative of the polarization versus time. The leakage current densities were measured from 5 to 200 kV/cm with a constant increment of 5 kV/cm in an unswitched linear type. A total of 30 s of 100 kV/cm DC bias were stressed for presetting the sample in a certain direction of polarization. The fatigue properties were measured using a 1 kHz square wave form with switching electric field of 100 kV/cm. $P−E$ hysteresis loops with $E_{max}$ of 200 kV/cm were performed after several switching cycles as indicated in the section.

## 3. Results and Discussion

**3.1 Synthesis.** The modified citrate-gel process is illustrated in Figure 1. Finding or preparing proper water-soluble metal

$Bi_{3.25}Pr_{0.75}Ti_{2.97}V_{0.03}O_{12}$ Ferroelectric Ceramics

*J. Phys. Chem. C, Vol. 111, No. 29, 2007* **11097**



**Figure 2.** XRD powder patterns of carbonized gels calcined at (a) 450 (*$Bi_2O_3$), (b) 500, (c) 550, (d) 600, and (e) 700 °C for 1 h (space group *Aba*2).

salts is a prerequisite for the citrate-gel method. Bismuth citrate and praseodymium acetate are commercially available and can be dissolved in water (the former needs the help of aqueous ammonium hydroxide, Figure 1, solution 1). The vanadium citrate solution was prepared by dissolving $V_2O_5$ and citric acid in water (Figure 1, solution 2). The as-prepared vanadium citrate solution was slightly dark green in color because of the reduction of $V^{5+}$ into $V^{3+}$ with citric acid. For the titanium source, a H-acac modified $Ti(O\text{-}n\text{-}Bu)_4$ solution in ethanol was used to reduce the moisture sensitivity of the titanium precursor solution (Figure 1, solution 3). A clear precursor solution was formed when a proper total amount of ethanol was used. A too small amount of ethanol will lead to two liquid phases while too much will cause precipitation. These phenomena can be explained by the hydrophobicity of the Ti-acac complex and the low solubility of metal citrates in ethanol. There is no separation step such as centrifugation or filtration in the whole citrate-gel process; therefore, the composition of the solid is close to that of the starting gel composition. However, a small excess of bismuth is advantageous as discussed below. The citrate-gel process can be performed at ambient conditions allowing for convenient and feasible processing.

The gel is subsequently carbonized to give an amorphous intermediate. Figure 1b shows the TG-DSC curves of the carbonized solid. About 6% weight loss was observed within the range of temperature from 100 to 150 °C resulting from the loss of adsorbed water. The exothermal peak at 404 °C was attributed to the decomposition of coordinated carboxyl groups, accompanied by 18% of weight loss. The strongest exothermal peak (46% weight loss) was observed at 462 °C. The powder calcined at 400 °C for 1 h was still a black amorphous substance. However, peaks in the XRD pattern of the powder obtained at 450 °C for 1 h can be attributed to crystalline $Bi_4Ti_3O_{12}$ (Figure 2a). The exothermal peak at 462 °C probably results from the burning of carbon produced by the decomposition of $-CH_x$ groups. The crystallization might be promoted by the released combustion enthalpy of the carbon, causing a low crystallization temperature of 450 °C.

Figure 2 shows the XRD patterns of calcined powders. The peak width decreases and the peak intensity increases with the calcination temperature. Below 450 °C, the calcined product was X-ray amorphous. A small impurity peak attributed to $Bi_2O_3$, as marked by a star in Figure 2, was observed; that might be attributed to the excess of bismuth used for compensation of bismuth loss during the sintering process. No impurity peak

was detected after calcination above 500 °C, and all reflections can be well-indexed to the $Bi_4Ti_3O_{12}$ structure despite some shifting, overlapping, or changing of intensity observed. The above observations are in agreement with a direct transformation of the amorphous carbonized solid into a crystalline phase with $Bi_4Ti_3O_{12}$ structure. An intermediate phase, such as the pyrochlore phase, was not observed.

The morphology and microstructure of the powder and ceramic was characterized by SEM. Figure 3a shows a typical SEM image of a powder sample synthesized at 500 °C. The particles are relatively uniform in size. The high magnification SEM image is shown in the inset, from which the particles can be observed more clearly. Investigation of various regions of the sample gave similar results with respect to the particle size and shape. The size distribution of the particle observed in the SEM image is given in Figure 3b from counting 100 randomly selected particles. The size of the particles ranged from 30 to 100 nm with a mean size of about 57 nm and a standard deviation of 14 nm. Figure 3c shows the SEM images of a ceramic sample, showing a uniform and dense structure. The grains in the ceramic were plate-like particles as observed in the high magnification SEM image in the inset of Figure 3c. No pores or cracks were observed. The dark areas in the SEM image are from the surface of crystallites while the light areas correspond to the edges. From the SEM images, it was found that the platelets were randomly arranged in the ceramic. No preferred orientation is observed. The composition of the ceramic was characterized by EDS given in Figure 3d. The atomic ratio for Bi:Pr:Ti measured was 3.25:0.76:2.85 and was close to the desired value of 3.25:0.75:2.97.

**3.2. Structure Refinement.** According to powder neutron diffraction experiments, $Bi_4Ti_3O_{12}$ is orthorhombic and crystallizes in the space group *B2cb* (standard setting *Aba*2) at room temperature.[48] However, an agreement on the structure of lanthanoid-substituted $Bi_4Ti_3O_{12}$ has not been reached. Chon et al. has suggested a tetragonal structure for the praseodymium-substituted bismuth titanate ($Bi_{4-x}Pr_xTi_3O_{12}$, $x = 0.85$) showing no peak splitting of (*h0l*)- and (0*kl*)-type reflections in the powder XRD data.[24] Garg et al. confirmed the orthorhombic structure for Nd-substituted bismuth titanate ($Bi_{4-x}Nd_xTi_3O_{12}$, $x = 0.85$) by the observation of the (014), (125), and (034) reflections using neutron powder diffraction.[25] In the case of La-substituted bismuth titanate ($Bi_{4-x}La_xTi_3O_{12}$, $x = 0.5$), Jeon et al. suggested a monoclinic *B1a1* space group being more suitable according to the final weighted *R* factors ($R_{wp}$) and the goodness-of-fit indicators ($S = R_{wp}/R_{exp}$) of a combined refinement of neutron and X-ray powder diffraction data.[49] On the other hand, a larger remanent polarization of 32 $\mu C/cm^2$ has been observed in highly *a* axis oriented $Bi_{4-x}La_xTi_3O_{12}$ ($x = 0.75$) films,[20] which was comparable with the $P_r$ value of 36 $\mu C/cm^2$ measured in parallel to the *ab* plane of $Bi_{4-x}La_xTi_3O_{12}$ ($x = 0.45$) of a single crystal.[50] Meanwhile, large $P_r$ values (50 $\mu C/cm^2$ for $Bi_{4-x}Nd_xTi_3O_{12}$, $x = 0.85$) were also observed in *c* axis oriented films.[23]

Considering the relation between the ferroelectric properties and crystal structure and the lack of consensus on the structure of lanthanoid-substituted $Bi_4Ti_3O_{12}$, we have used the Rietveld method to refine the crystal structure of as-prepared BPTV. The structure models used for the Rietveld refinement were built by partially occupying the perovskite A site with $Pr^{3+}$ in the $Bi_4Ti_3O_{12}$ crystal structures. The ICSD data (No. 240210) were used as initial parameters for the orthorhombic $Bi_4Ti_3O_{12}$ structure refinement. Vanadium was not taken into account because of its low substitution level and atomic number being
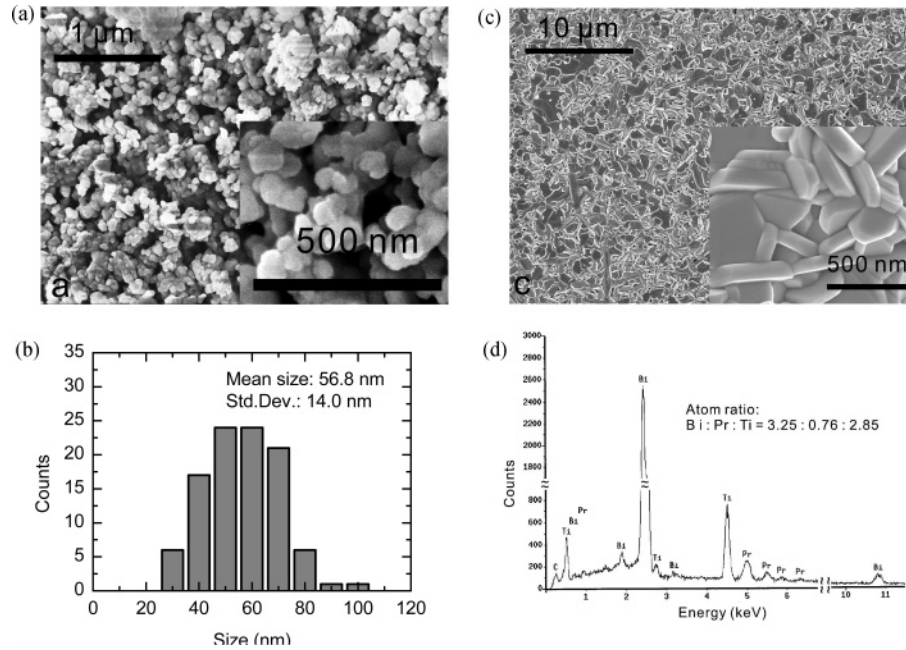
**Figure 3.** (a) SEM image of as prepared BPTV powder (inset: high magnification), (b) size distribution for randomly selected 100 particles in (a), (c) SEM image of the BPTV ceramic (inset: high magnification), and (d) EDS spectrum from (c).

**TABLE 1: Refined Lattice Parameters of BPTV Ceramic in Space Group $Aba2^a$**

|                            | refined        | ICSD #240210  |
| -------------------------- | -------------- | ------------- |
| $a$ (Å)                    | 5.4060(3)      | 5.41014(11)   |
| $b$ (Å)                    | 32.8492(2)     | 32.8565(7)    |
| $c$ (Å)                    | 5.4145(8)      | 5.44513(11)   |
| $V$ (Å$^3$)                | 961.54(2)      | 967.91(9)     |
| $\rho_{calc}$ (g/cm$^3$)   | 7.741          |               |
| $R_{wp}$ (%)               | 5.01           |               |
| $R_p$ (%)                  | 4.24           |               |
| dwd                        | 1.134          |               |
| reduced $\chi^2$           | 1.430          |               |
| variables                  | 25             |               |
| wave length                | Cu K$\alpha$1  |               |
| geometry                   | transmission   |               |
| monochromator              | Ge(111)        |               |
| $T$ (K)                    | 298            |               |

$^a$ Parameters were transformed from space group $B2cb$ to $Aba2$ by rotating axes and coordinates according to $abc = b'c'a'$.

**TABLE 2: Refined Atomic Parameters in Space Group $Aba2$**

| atom | x          | y          | z         | occupancy | uiso (Å$^2$) |
| ---- | ---------- | ---------- | --------- | --------- | ------------ |
| Pr1  | 0.9966(4)  | 0.0668(7)  | 0.00000   | 0.375     | 0.019(0)     |
| Bi1  | 0.9966(4)  | 0.0668(7)  | 0.00000   | 0.625     | 0.019(0)     |
| Bi2  | 0.0167(5)  | 0.2109(9)  | 0.0062(2) | 1.0       | 0.022(5)     |
| Ti1  | 0.00000    | 0.50000    | 0.0329(9) | 1.0       | 0.011(4)     |
| Ti2  | 0.0047(2)  | 0.3717(6)  | 0.0308(9) | 1.0       | 0.011(0)     |
| O1   | 0.2626(0)  | 0.0084(2)  | 0.3110(9) | 1.0       | 0.005(2)     |
| O2   | 0.2469(6)  | 0.2499(3)  | 0.2636(6) | 1.0       | 0.001(7)     |
| O3   | 0.0723(2)  | 0.4415(8)  | 0.0589(8) | 1.0       | 0.003(9)     |
| O4   | 0.9506(2)  | 0.3189(6)  | 0.0392(9) | 1.0       | 0.001(2)     |
| O5   | 0.2302(2)  | 0.1124(6)  | 0.2734(9) | 1.0       | 0.011(8)     |
| O6   | 0.2984(2)  | 0.8761(6)  | 0.3431(9) | 1.0       | 0.001(6)     |

similar to that of the substituted titanium. The atomic coordinates and isotropic atomic displacement parameters were refined. The atomic occupancy of Bi/Pr was fixed at 0.375/0.625 presuming the ratio of Bi/Pr was 3.25:0.75. After refinement, the structure was transformed from space group $B2cb$ to $Aba2$ by rotating axes and coordinates according to $abc = b'c'a'$. The refined lattice and atomic parameters are listed in Tables 1 and 2. Figure 4 gives the refined profiles of the XRD powder pattern of BPTV

using a pseudo-Voigt peak function. The refined profile results in a good fit for the experimental data. As seen in the inset of Figure 4, the (140) diffraction peak in the space group $Aba2$ ((014) in $B2cb$) is detected. This result is consistent with Garg et al.'s observation in $Bi_{4-x}Nd_xTi_3O_{12}$ ($x = 0.85$).[25] The final weighted $R$ value ($R_{wp}$) and the goodness-of-fit ($\chi^2$) for the orthorhombic structure were 5.01% and 1.430, respectively, as listed in Table 1. Chon et al. have suggested a tetragonal structure for $Bi_{4-x}Pr_xTi_3O_{12}$ ($x = 0.85$).[24] However, no atomic coordinates, temperature factors, and atomic occupancies are provided in their report. The monoclinic structure suggested for $Bi_4Ti_3O_{12}$[49] did not result in a convergent refinement for the cosubstituted samples reported in this work.

As listed in Table 1, the final refined cell parameters were $a = 5.4060(3)$ Å, $b = 32.8492(2)$ Å, $c = 5.4145(8)$ Å, and $V = 961.54(2)$ Å$^3$ in the space group $Aba2$. As compared with $Bi_4Ti_3O_{12}$, only a small decrease of the lattice constants (0.0041, 0.0073, and 0.0305 Å for $a$, $b$, and $c$) was observed, resulting in a slight decrease of 6.38 Å$^3$ for the cell volume. The decrease of the $c$ ($a$ for $B2cb$) parameter and the cell volume for BPTV is consistent with the same trend observed in $Pr^{3+}$,[24] $Nd^{3+}$,[23] and $La^{3+}$ [50] substituted $Bi_4Ti_3O_{12}$. This might be attributed to the larger effective radii of 1.17 Å for $Bi^{3+}$ cations rather than that of 1.126 Å for $Pr^{3+}$ cations with a coordination number of 8.[51] Figure 5 presents the crystal structure of BPTV projected along different directions using the final refined parameters. Even though absorption correction in transmission geometry is a concern for materials containing heavy atoms, the refinement resulted in satisfactory $R$ values.

**3.3. Ferroelectric Properties.** The as-prepared BPTV ceramic shows a well-saturated $P-E$ hysteresis loop, as seen in Figure 6a. The $2P_r$ and $2E_c$ values were 35 $\mu$C/cm$^2$ and 148 kV/cm, respectively. The switch current density reached a maximum value at the drive field of about $\pm E_c$ (Figure 6b). A comparison between the BPTV ceramic and the other lead-free ferroelectric bulk ceramics and thin films is given in Table 3. The polarization $P_r$ obtained in our work is comparable to reported values, 12−19 and 8.5−17 $\mu$C/cm$^2$ for $Bi_{3.5}Pr_{0.5}(Ti,V)_3O_{12}$[21] and $(Bi, La)_4(Ti,V)_3O_{12}$[21,28] films, respectively. However, the $P_r$ of the BPTV ceramic is lower than that of
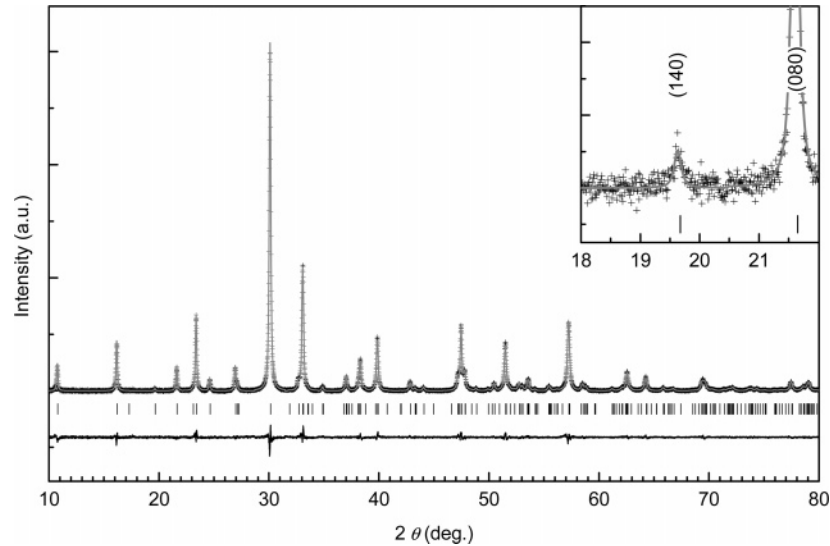
**Figure 4.** Difference plots of the BPTV ($x = 0.75$, $y = 0.03$) ceramic after the Rietveld refinement based on the orthorhombic model using space group *Aba*2, inset shows (140) diffraction peak.
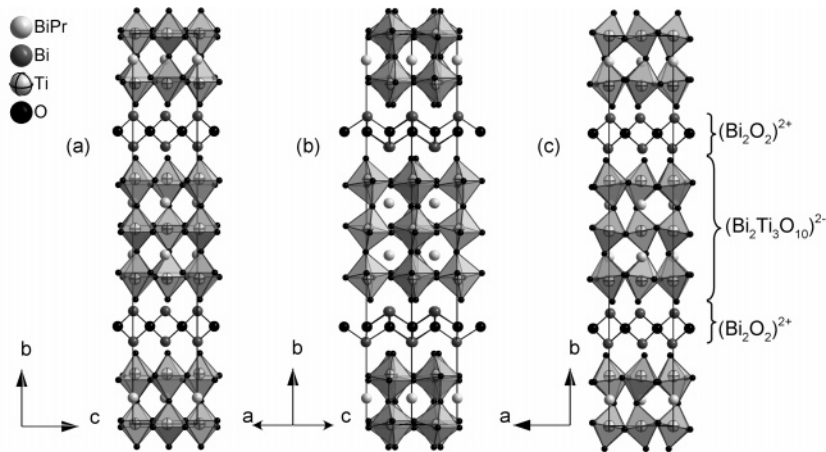


**Figure 5.** Refined BPTV crystal structure viewed along (a) [100], (b) [101], and (c) [001] directions.

**TABLE 3: Comparison of the Properties for BPTV Ceramics and Other Lead-Free Ferroelectric Bulk Ceramics and Thin Films**

| composition | shape | $P_r$ ($\mu$C/cm$^2$) | $E_c$ (kV/cm) | $E_{max}$ (kV/cm) | growth method | growth condition |
|---|---|---|---|---|---|---|
| Bi$_{3.5}$Pr$_{0.5}$(Ti,V)$_3$O$_{12}$ | film | 12–19 | 114–132 | 400 | CSD[21] | 750 °C, 5 min |
| (Bi, La)$_4$(Ti,V)$_3$O$_{12}$ | film | 8.5–17 | 48–135 | 300–400 | CSD,[21] MOCVD[28] | 680–750 °C |
| Bi$_{3.5}$Nd$_{0.5}$Ti$_{2.98}$V$_{0.02}$O$_{12}$ | film | 37 | 116 | 400 | CSD[11, 21] | 750 °C, 5 min |
| Bi$_4$Ti$_3$O$_{12}$ | ceramic | 13 | 30 | 200 | solid-state reaction[9] | 850 °C, 2 h, O$_2$ |
| Bi$_4$(Ti,V,W)$_3$O$_{12}$ | ceramic | 18–20 | ~40 | 200 | solid-state reaction[9,10] | 1050 °C, 2 h |
| Bi$_{0.5}$(Na$_{0.8}$K$_{0.2}$)$_{0.5}$TiO$_3$ | ceramic | 20 | ~3 | 4 | solid-state reaction[52] | 1100 °C, 2 h |
| (Bi$_{0.5}$Na$_{0.5}$)$_{0.94}$Ba$_{0.06}$TiO$_3$ | ceramic | ~20 | | | solid-state reaction[53] | 1200 °C, 2 h |
| SrBi$_2$Ta$_2$O$_9$ | ceramic | 7.6 | 22 | ~40 | sol–gel[54] | 1200 °C, 8 h |
| SrBi$_4$Ti$_4$O$_{15}$ | ceramic | 8 | 42.5 | 80 | citrate-nitrate gel[55] | 1060 °C, 1 h |
| Bi$_{3.25}$Pr$_{0.75}$Ti$_{2.97}$V$_{0.03}$O$_{12}$ | ceramic | 17 | 74 | 300 | citrate-gel[a] | 900 °C, 4 h |
| Bi$_{3.25}$Pr$_{0.75}$Ti$_3$O$_{12}$ | ceramic | 12 | 58 | 250 | citrate-gel[a] | 900 °C, 4 h |

*[a] This work.*

37 $\mu$C/cm$^2$ observed in the Bi$_{3.5}$Nd$_{0.5}$Ti$_{2.98}$V$_{0.02}$O$_{12}$ film.[11,21] This can be explained by the larger structural distortion resulting from Nd$^{3+}$ substitution as compared with Pr$^{3+}$ substitution,[21,25] because the ionic radius of Nd$^{3+}$ (1.109 Å) is smaller than that of Pr$^{3+}$ (1.126 Å) for a coordination number of 8.[51] Compared with other lead-free ceramics, the $P_r$ of the prepared BPTV ceramic is comparable to that of pure Bi$_4$Ti$_3$O$_{12}$,[9] Bi$_4$-(Ti,V,W)$_3$O$_{12}$,[9,10] Bi$_{0.5}$(Na$_{0.8}$K$_{0.2}$)$_{0.5}$TiO$_3$,[52] and (Bi$_{0.5}$Na$_{0.5}$)$_{0.94}$-Ba$_{0.06}$TiO$_3$[53] ceramics (Table 3) and is nearly twice the value observed for sol–gel derived SrBi$_2$Ta$_2$O$_9$[54] and citrate–nitrate gel derived SrBi$_4$Ti$_4$O$_{15}$[55] ceramics. The measurements of $2P_r$

and $2E_c$ were carried out for different ceramic samples with identical composition and on different areas of the same ceramic showing good reproducibility. The saturation properties were characterized by the evolution of $2E_c$, $2P_r$, and $P_{max}$ with $E_{max}$. As seen in Figure 7a, the $2E_c$, $2P_r$, and $P_{max}$ showed similar behavior. Their values show a pronounced increase within the range of $E_{max}$ from 50 to 100 kV/cm, whereas above ($E_{max} >$ 100 kV/cm) a more gradual increase was observed. These saturation properties were more apparent in the first derivative shown in Figure 7b. The values of d($2P_r$)/d($E_{max}$) and d($P_{max}$)/d($E_{max}$) had maxima at the same $E_{max}$ of 80 kV/cm, and 70 kV/
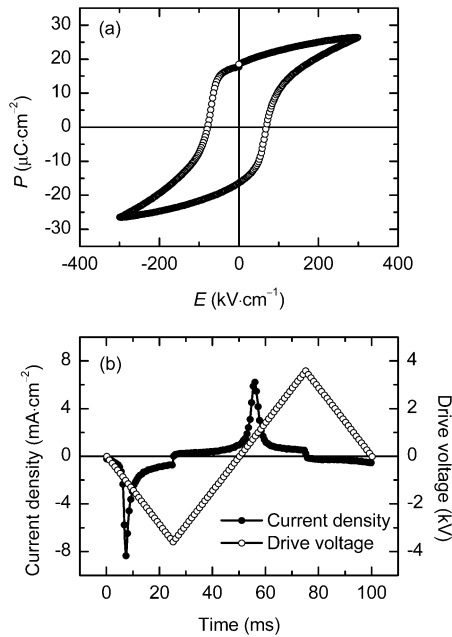
**Figure 6.** (a) $P-E$ hysteresis loop of as-prepared ceramic and (b) curves of switching current density and drive voltage as functions of time.

cm for that of $d(2E_c)/d(E_{max})$. These values are coincidentally close to the $E_c$ of 74 kV/cm from the hysteresis with 300 kV/cm of $E_{max}$, as shown in Figure 6. This coincidence is confirmed using an ideal ferroelectric capacitor model,[56] in which the ferroelectric has a field independent dielectric constant ($\epsilon_{fe}$) and an ideal switching behavior (the ferroelectric polarization is zero below $E_c$ and has a constant value ($P_s$, spontaneous polarization) above $E_c$). The electric displacement ($D$) in the ideal ferroelectric capacitor therefore consists of two components and can be expressed as:

$$D = P_s + \epsilon_0 \cdot \epsilon_{fe} \cdot E \tag{1}$$

where $\epsilon_0$ is the vacuum permittivity. Figure 7c shows the hysteresis loop based on the ideal ferroelectric capacitor model. Obviously, the measured $2E_c$ and $2P_r$ ($P_r$ equals $P_s$ in the ideal model) are zero below $E_c$ and have a constant value above $E_c$, while the $P_{max}$ (measured $D$ value) has a linear relationship with the electric field but an abrupt increase at $E_c$ (Figure 7d). Their differentiated curves will have sharp peaks at $E_c$, as illustrated in Figure 7e. In a ceramic sample, these peaks are broadened because of different domains with different $E_c$ (caused by domain pinning) and a different polarization (caused by domain orientation). Therefore, the peak positions observed in the experimental plots of $d(2P_r)/d(E_{max})$, $d(P_{max})/d(E_{max})$, and $d(2E_c)/d(E_{max})$ indicate statistical values in terms of $E_c$, suggesting the validity of using these plots within a range of relatively low $E_{max}$ to estimate the $E_c$ value at highly saturated conditions (or denoted as saturated $E_c$). This treatment has advantages, especially in two cases. One case is that a material with larger $E_c$ makes it difficult to achieve saturated hysteresis loops. The other case is a material with a low breakdown electric field resulting from a high leakage current. In the latter case, failure of measurement will occur before a saturation is observed in the hysteresis loop. In both cases, it will be difficult to get the saturated $E_c$ value directly from a $P-E$ hysteresis loop measurement.

The saturation properties can also be expressed by using the ratio of $P_{max}/P_r$. As seen in Figure 8a, the value of $P_{max}/P_r$

decreases with $E_{max}$ but reaches a constant value above 75 kV/cm of $E_{max}$, in agreement with the $E_c$ obtained from the saturated hysteresis loop as discussed above. The inset of Figure 8a shows that $P_{max}/P_r$ increases linearly with $E_{max}$ at $E_{max} > 100$ kV/cm. The linear relationship is held above $E_c$ in an ideal ferroelectric capacitor as obtained from eq 1:

$$\frac{P_{max}}{P_r} = \frac{P_{max}}{P_s} = 1 + \frac{\epsilon_0 \cdot \epsilon_{fe}}{P_s} \cdot E_{max} \tag{2}$$

in which the y intercept equals one and the slope equals $\epsilon_0 \cdot \epsilon_{fe}/P_s$. As far as a real ferroelectric ceramic capacitor is concerned, four current sources should be taken into account (a four parallel components model[57]): remanent polarization produced by uncoupled domains ($P_r$ from $C_r$), nonremanent polarization due to coupled domains in a ferroelectric capacitor ($P_{nr}$ from $C_{nr}$), parallel parasitic capacitance from field independent dielectric constant ($C_p$: $\epsilon_0 \cdot \epsilon_{fe} \cdot E$), and resistive leakage ($J$ from $R$), as illustrated in Figure 8b. According to this model, the latter three are nonremanent. The measured $P_{max}$ therefore can be expressed using these four components (Figure 8c):
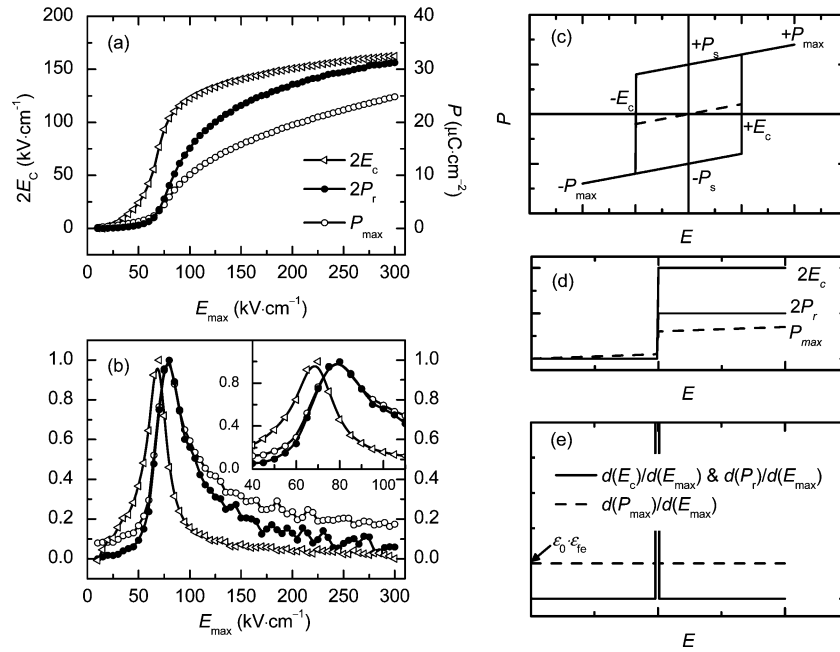
$$P_{max} = P_r + P_{nr} + \epsilon_0 \cdot \epsilon_{fe} \cdot E_{max} + \int J(t)dt \tag{3}$$

For a low leakage current ferroelectric material, the contribution of the last component can be omitted. Therefore, the value of $P_{max}/P_r$ is deduced as:

$$\frac{P_{max}}{P_r} = 1 + \frac{P_{nr}}{P_r} + \frac{\epsilon_0 \cdot \epsilon_{fe}}{P_r} \cdot E_{max} \tag{4}$$

When the $E_{max}$ is lower than $E_c$, few domains can be switched by such low electric field; thereby, both $P_r$ and $P_{nr}$ are close to zero. So the value of $P_{max}/P_r$ is dominated by $E_{max}/P_r$. This is consistent with the result in the low electric field range as observed in Figure 8a. On the other hand, when the $E_{max}$ is above $E_c$, both $P_r$ and $P_{nr}$ will increase with $E_{max}$. The ratio of $P_{nr}$ and $P_r$ might be close to a constant that is predetermined by the fractions of coupled and free (or switchable) domains, which are dependent on both the composition and the preparation. On the basis of the above hypothesis, a linear plot can be obtained only if $\epsilon_0 \cdot \epsilon_{fe}/P_r$ is also close to a constant. With presumption of $\epsilon_{fe}$ about 300, the value of $\epsilon_0 \cdot \epsilon_{fe}/P_r$ was 3.8$-$1.6 × $10^{-3}$ (cm/kV) when the $P_r$ increases from 7 to 17 $\mu$C/cm$^2$ as observed at about 100 and 300 kV/cm in this work. The $\epsilon_0 \cdot \epsilon_{fe}/P_r$ shows only a slight decrease with increasing $E_{max}$ within the high electric field range; therefore, a linear relationship between $P_{max}/P_r$ and $E_{max}$ will be obtained. The linear part of the plot of $P_{max}/P_r$ versus $E_{max}$ has a y intercept $B = 1 + (P_{nr}/P_r)$ and a slope of $\epsilon_0 \cdot \epsilon_{fe}/P_r$. Thus, the y intercept allows for the estimation of $P_{nr}/P_r = B - 1$. For the studied BPTV ceramic, $\epsilon_{fe}$ and $P_{nr}$ were 283 and 2.7 $\mu$C/cm$^2$ calculated from the fitted values of slope and y intercept using the measured $P_r$ of 17.5 $\mu$C/cm$^2$ at $E_{max}$ of 300 kV/cm. The linear dielectric constant of 283 is reasonable for a ferroelectric Bi$_4$Ti$_3$O$_{12}$ based material that normally is around 200 at room temperature, and $P_{nr}$ of 2.7 $\mu$C/cm$^2$ is very low in comparison with 17.5 $\mu$C/cm$^2$ for $P_r$, indicating a low degree of coupling of the domains in the sample. For the studied BPTV, the value of $P_{nr}/P_r$ from eq 4 equals 0.153 using the measured $P_r$ of 17.5 $\mu$C/cm$^2$ at $E_{max}$ of 300 kV/cm. This value could be used as a factor to characterize the level or extent of domain coupling.

Figure 9a presents the logarithmic scale $J-E$ curves, showing symmetric leakage current density. It was found that $J$ was linear with $E$ within a range of ±300 kV/cm (Figure 9b). The sudden

Bi$_{3.25}$Pr$_{0.75}$Ti$_{2.97}$V$_{0.03}$O$_{12}$ Ferroelectric Ceramics

*J. Phys. Chem. C, Vol. 111, No. 29, 2007* **11101**



**Figure 7.** (a) $2E_c$, $2P_r$, and $P_{max}$ as a function of $E_{max}$, (b) normalized plots of d($2E_c$)/d($E_{max}$) (triangle), d($2P_r$)/d($E_{max}$) (hollow circle), and d($P_{max}$)/d($E_{max}$) (solid circle, inset: details of the peaks), and plots from the ideal ferroelectric capacitor model: (c) hysteresis loop (dashed line, below $E_c$; solid line, above $E_c$), (d) $2E_c$, $2P_r$ ($P_r = P_s$), and $P_{max}$ vs $E_{max}$, and (e) differentiated curves of (d).
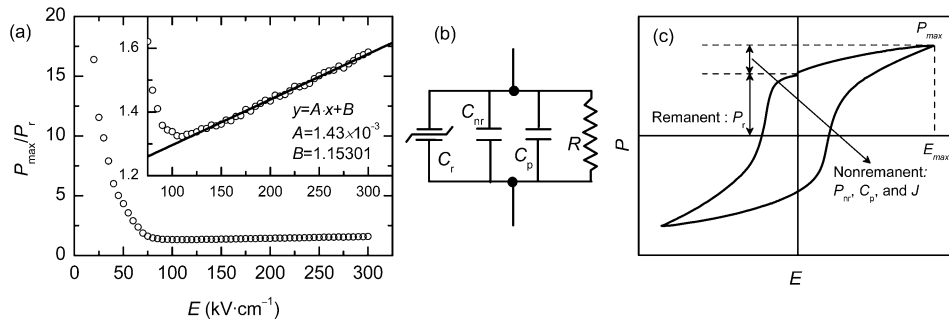


**Figure 8.** (a) Plots of $P_{max}/P_r$ vs $E_{max}$ and inset: linear fitted plots, (b) four components model for a ferroelectric capacitor, and (c) illustration of contributions of four components to $P_{max}$.
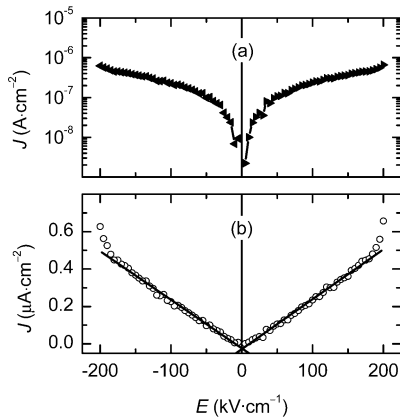


**Figure 9.** Room temperature $J-E$ plots of the BPTV ceramic: (a) logarithmic scale and (b) linear scale (circles, experiment; solid line, linear fit).

increase of $J$ around $\pm200$ kV/cm might due to a change of the conductive mechanism. However, a breakdown is unlikely because after the leakage measurement the hysteresis loop almost has no change. The typical leakage current density was below 1 $\mu$A/cm$^2$. On the basis of the measured leakage current density, the contribution of leakage to the $P_{max}$ should be much lower than 0.1 $\mu$C/cm$^2$. Therefore, neglecting the contribution

of leakage current to the $P_{max}$ in the four components model as discussed above was a valid assumption. The low leakage current density might be due to a reduced number of oxygen vacancies caused by the substitution of Pr$^{3+}$ and V$^{5+}$.

Fatigue measurements show a high endurance for the as-prepared BPTV ceramic. As seen in Figure 10a, there was no significant decrease of $\pm P_r$ after switching over $10^8$ cycles. A slight increase of $\pm P_r$ was observed around $10^6$ switching cycles. Figure 10b gives the hysteresis loops measured before and after the fatigue test, resulting in almost the same $\pm P_r$ and $\pm P_{max}$. This provides further evidence for the high fatigue endurance of the as-prepared BPTV ceramic. A small difference between the two hysteresis loops was a little decrease of $-E_c$ for the hysteresis loop measured after the fatigue test.

V$^{5+}$ substitution has been found to be important to improve $P_r$ in this work. The ceramic of Bi$_{3.25}$ Pr$_{0.75}$Ti$_3$O$_{12}$ (BPT) was also prepared using the same method for comparison. As seen in Figure 11, the $2P_r$ of the BPT ceramic was 24 $\mu$C/cm$^2$ at $E_{max}$ of 250 kV/cm, which is smaller than that of BPTV (30$\mu$C/ cm$^2$). A slight increase of the coercive field was observed with V$^{5+}$ substitution. However, we failed to obtain a $P-E$ hysteresis loop with $E_{max}$ of 300 kV/cm for BPT ceramic before the breakdown of the sample. There are two possible ways for V$^{5+}$ substitution that can contribute to improve the ferroelectric properties, in particular, to increase $P_r$. Domain pinning was
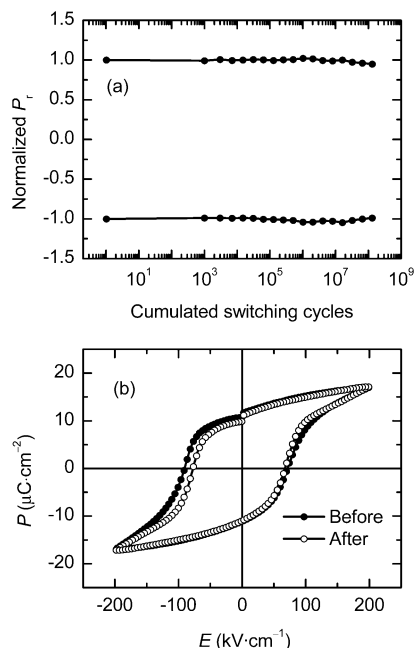
**Figure 10.** (a) Plots of $P_r$ vs cumulated switching cycles and (b) hysteresis loop before (solid) and after (hollow) $10^8$ switching cycles.
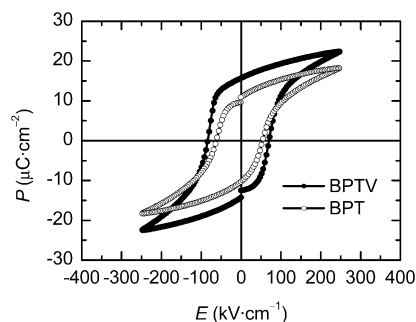


**Figure 11.** Comparison of $P-E$ hysteresis loops between BPTV and BPT ceramics at $E_{max}$ of 250 kV/cm.

supposed to be suppressed because of the $V^{5+}$ substitution causing a decrease of the space charge density through compensating oxygen vacancies.[9,10,21] On the other hand, substitution of $Ti^{4+}$ (0.605 Å) by smaller $V^{5+}$ (0.54 Å) may cause a local lattice distortion, which may be in favor of an increase of $P_r$ in a similar way as substitutions by lanthanide cations having smaller ionic radii than $Bi^{3+}$.[25] The effect of local lattice distortion caused by $V^{5+}$ substitution may be less important than that of suppression of domain pinning by compensating oxygen vacancies due to the low substitution level.[29]

## 4. Conclusions

Praseodymium and vanadium cosubstituted $Bi_4Ti_3O_{12}$ were synthesized using a modified citrate-gel method. The crystallization was observed as low as 450 °C. The carbonized amorphous precursor was directly transformed into crystalline BPTV with the $Bi_4Ti_3O_{12}$ structure. The synthesized powder was of uniform particle size ranging from 30 to 100 nm. The mean size was 57 nm with a standard deviation of 14 nm. The ceramic prepared from the as-synthesized powder consisted of randomly arranged platelets with a thickness of about 200 nm.

Ferroelectric measurements show that the as-prepared ceramics have good ferroelectric properties. A saturated $P-E$ hysteresis loop was obtained from the as-prepared ceramic. The

$2P_r$ and $2E_c$ values measured at 300 kV/cm were 35 $\mu C/cm^2$ and 148 kV/cm, respectively. The observed linear relationship between $P_{max}/P_r$ and $E_{max}$ was interpreted as ideal and a four components ferroelectric capacitor model for the calculation of the field independent dielectric constant and nonremanent polarization. For the BPTV ceramic studied, the calculated field independent dielectric constant was 282, and the calculated nonremanent polarization resulting from coupled domains was 2.7 $\mu C/cm^2$ at $E_{max} = 300$ kV/cm. The as-prepared ceramic shows ohmic conductivity. The current density was found to be below 1 $\mu A/cm^2$. No significant decrease of $P_r$ was observed after switching over $10^8$ cycles. The well-saturated hysteresis loop, low leakage, and low fatigue is promising for applications in devices.

**References and Notes**

(1) Sugibuchi, K.; Kurogi, Y.; Endo, N. *J. Appl. Phys.* **1975**, *46*, 2877.
(2) Bondurant, D. W.; Gnadinger, F. P. *IEEE Spectrum* **1989**, *26*, 30.
(3) Damjanovic, D. *Rep. Prog. Phys.* **1998**, *61*, 1267.
(4) Dimos, D.; Mueller, C. H. *Annu. Rev. Mater. Sci.* **1998**, *28*, 397.
(5) Dimos, D. *Annu. Rev. Mater. Sci.* **1995**, *25*, 273.
(6) Aurivillius, B. *Ark. Kemi* **1950**, *1*, 499.
(7) de Araujo, C. A. P.; Cuchiaro, J. D.; McMillan, L. D.; Scott, M. C.; Scott, J. F. *Nature* **1995**, *374*, 627.
(8) Park, B. H.; Kang, B. S.; Bu, S. D.; Noh, T. W.; Lee, J.; Jo, W. *Nature* **1999**, *401*, 682.
(9) Noguchi, Y.; Miwa, I.; Goshima, Y.; Miyayama, M. *Jpn. J. Appl. Phys.* **2000**, *39*, L1259.
(10) Noguchi, Y.; Miyayama, M. *Appl. Phys. Lett.* **2001**, *78*, 1903.
(11) Uchida, H.; Yoshikawa, H.; Okada, I.; Matsuda, H.; Iijima, T.; Watanabe, T.; Kojima, T.; Funakubo, H. *Appl. Phys. Lett.* **2002**, *81*, 2229.
(12) Yamada, M.; Iizawa, N.; Yamaguchi, T.; Sakamoto, W.; Kikuta, K.; Yago, T.; Hayashi, T.; Hirano, S.-i. *Jpn. J. Appl. Phys.* **2003**, *42*, 5222.
(13) Uitert, L. G. V.; Egerton, L. *J. Appl. Phys.* **1961**, *32*, 959.
(14) Subbarao, E. C. *Phys. Rev.* **1961**, *122*, 804.
(15) Cummins, S. E.; Cross, L. E. *J. Appl. Phys.* **1968**, *39*, 2268.
(16) Irie, H.; Miyayama, M.; Kudo, T. *J. Appl. Phys.* **2001**, *90*, 4089.
(17) Si, J.; Desu, S. B. *J. Appl. Phys.* **1993**, *73*, 7910.
(18) Wang, H.; Fu, L. W.; Shang, S. X. *J. Appl. Phys.* **1993**, *73*, 7963.
(19) Yamaguchi, M.; Nagatomo, T.; Omoto, O. *Jpn. J. Appl. Phys.* **1997**, *36*, 5885.
(20) Lee, H. N.; Hesse, D.; Zakharov, N.; Gösele, U. *Science* **2002**, *296*, 2006.
(21) Uchida, H.; Yoshikawa, H.; Okada, I.; Matsuda, H.; Iijima, T.; Watanabe, T.; Funakubo, H. *Jpn. J. Appl. Phys.* **2002**, *41*, 6820.
(22) Sun, Y.; Chen, Y.; Gan, J.; Hwang, J. *Jpn. J. Appl. Phys.* **2002**, *41*, L892.
(23) Chon, U.; Jang, H. M.; Kim, M. G.; Chang, C. H. *Phys. Rev. Lett.* **2002**, *89*, 087601.
(24) Chon, U.; Shim, J. S.; Jang, H. M. *J. App. Phys.* **2003**, *93*, 4769.
(25) Garg, A.; Barber, Z. H.; Dawber, M.; Scott, J. F.; Snedden, A.; Lightfoot, P. *Appl. Phys. Lett.* **2003**, *83*, 2414.
(26) Matsuda, H.; Ito, S.; Iijima, T.; Mashimo, T.; Okino, H.; Yamamoto, T. *Jpn. J. Appl. Phys.* **2004**, *43*, 6689.
(27) Simoes, A. Z.; Gonzaiez, A. H. M.; Riccardi, C. S.; Souza, E. C.; Moura, F.; Zaghete, M. A.; Longo, E.; Varela, J. A. *J. Electroceram.* **2004**, *13*, 65.
(28) Watanabe, T.; Funakubo, H.; Osada, M.; Noguchi, Y.; Miyayama, M. *Appl. Phys. Lett.* **2002**, *80*, 100.
(29) Uchida, H.; Okada, I.; Matsuda, H.; Iijima, T.; Watanabe, T.; Funakubo, H. *Jpn. J. Appl. Phys.* **2004**, *43*, 2636.
(30) Li, W.; Yin, Y.; Su, D.; Zhu, J. *J. App. Phys.* **2005**, *97*, 084102.
(31) Ohki, H.; Wang, X.; Ishiwara, H. *Jpn. J. Appl. Phys.* **2005**, *44*, 964.
(32) Chen, M.; Liu, Z. L.; Wang, Y.; Wang, C. C.; Yang, X. S.; Yao, K. L. *Phys. Status Solidi A* **2003**, *200*, 446.
(33) Chu, R. Q.; Zhang, L. N.; Xu, Z. J.; Zeng, H. R.; Yu, H. F.; Yin, Q. R. *Phys. Status Solidi A* **2004**, *201*, R45.
(34) Li, W.; Chen, A.; Lu, X.; Zhu, J. *J. Appl. Phys.* **2005**, *98*, 024109.
(35) Hardy, A.; Mondelaers, D.; Bael, M. K. V.; Mullens, J.; Poucke, L. C. V. *J. Eur. Ceram. Soc.* **2004**, *24*, 905.
(36) Dhage, S. R.; Khollam, Y. B.; Dhespande, S. B.; Potdar, H. S.; Ravi, V. *Mater. Res. Bull.* **2004**, *39*, 1993.

Bi$_{3.25}$Pr$_{0.75}$Ti$_{2.97}$V$_{0.03}$O$_{12}$ Ferroelectric Ceramics

*J. Phys. Chem. C, Vol. 111, No. 29, 2007* **11103**

(37) Liu, W. L.; Xia, H. R.; Han, H.; Wang, X. Q. *J. Mater. Sci.* **2005**, *40*, 1827.

(38) Du, Y. L.; Zhang, M. S.; Chen, Q.; Yuan, Z. R.; Yin, Z.; Zhang, Q. A. *Solid State Commun.* **2002**, *124*, 113.

(39) Shi, Y.; Cao, C.; Feng, S. *Mater. Lett.* **2000**, *46*, 270.

(40) Chen, D.; Jiao, X. *Mater. Res. Bull.* **2001**, *36*, 355.

(41) Yang, Q.; Li, Y.; Yin, Q.; Wang, P.; Cheng, Y.-B. *J. Eur. Ceram. Soc.* **2003**, *23*, 161.

(42) Pookmanee, P.; Uriwilast, P.; Phanichpant, S. *Ceram. Int.* **2004**, *30*, 1913.

(43) Du, H.; Wohlrab, S.; Kaskel, S. *J. Nanosci. Nanotechnol.* **2006**, *6*, 2110.

(44) Sale, F. R. In *The citrate-gel processing of electronic and magnetic ceramics*, IEE Colloquium on Sol-gel Materials for Device Applications, 1998; IEE: London, U.K.; pp 4/1.

(45) Schwartz, R. W. *Chem. Mater.* **1997**, *9*, 2325.

(46) Larson, A. C.; Dreele, R. B. V. *Gerneral Structure Analysis System (GSAS)*; Los Alamos National Analysis System, 2004.

(47) Toby, B. H. *J. Appl. Crystallogr.* **2001**, *34*, 210.

(48) Hervoches, C. H.; Lightfoot, P. *Chem. Mater.* **1999**, *11*, 3359.

(49) Jeon, M. K.; Kim, Y. I.; Nahm, S. H.; Woo, S. I. *J. Phys. Chem. B* **2005**, *109*, 968.

(50) Noguchi, Y.; Soga, M.; Takahashi, M.; Masaru, M. *Jpn. J. Appl. Phys.* **2005**, *44*, 6998.

(51) Shannon, R. *Acta Crystallogr., Sect. A* **1976**, *32*, 751.

(52) Sasaki, A.; Chiba, T.; Mamiya, Y.; Otsuki, E. *Jpn. J. Appl. Phys.* **1999**, *38*, 5564.

(53) Takenaka, T.; Maruyama, K.-i.; Sakata, K. *Jpn. J. Appl. Phys.* **1991**, *30*, 2236.

(54) Babooram, K.; Ye, Z.-G. *Chem. Mater.* **2006**, *18*, 532.

(55) Chu, R. Q.; Xu, Z. J.; Zhu, Z. Q.; Li, G. R.; Yin, Q. R. *Mater. Sci. Eng., B* **2005**, *122*, 106.

(56) Phintilie, L.; Alexe, M. *J. App. Phys.* **2005**, *98*, 124103.

(57) Evans, J. T.; Bullington, J. A. In *A ferroelectric capacitor simulation model*, IEEE 7th International Symposium on Applications of Ferroelectrics, 1990; pp 692.